VNU Journal of Science: Mathematics - Physics

Journal homepage: https://js.vnu.edu.vn/MaP

Original Article

Outstanding Bolometric Performance of $Y_3Fe_{4.96}Mo_{0.04}O_{12}$ Synthesized via Sol-Gel Method

Nguyen Phuc Duong[1], Dao Thi Thuy Nguyet[1*], Nguyen Thi Nguyen[1], Tran Thi Viet Nga[1], Luong Ngoc Anh[1], Le Tuan Tu[2]

[1]*School of Materials Science and Engineering, Hanoi University of Science and Technology, 1 Dai Co Viet, Hanoi, Vietnam*

[2]*VNU University of Science, 334 Nguyen Trai, Thanh Xuan, Hanoi, Vietnam*

Received 26th August 2025
Revised 4th December 2025; Accepted 6th April 2026

Abstract: The yttrium iron garnet (YIG) material doped with molybdenum (Mo^{5+}) with the composition $Y_3Fe_{4.96}Mo_{0.04}O_{12}$ (x = 0.04) was synthesized using a sol-gel method combined with thermal treatment. The resulting powder had a single-phase structure, high crystallinity, and a uniform microstructure. Morphological, structural, and electrical characteristics of the material were investigated using XRD, SEM, FTIR, and I–V measurements. A bolometer device was fabricated by depositing the YIG sensing layer onto an interdigitated Pt electrode array. Photo-current, responsivity (R_i), noise equivalent power (NEP), and specific detectivity (D^*) measurements were performed in the ultraviolet–visible–near-infrared (UV–VIS–NIR, 281–1010 nm) range. The x = 0.04 sample yielded an activation energy of 0.32 eV, a TCR of 3.9 $\%K^{-1}$, a photo-current of ~106 µA, and a responsivity of 848 mA/W. The NEP and D^* values were suitable for a sensor operating at room temperature without the need for cooling. The results were compared with other doped YIG samples, such as $Y_3Fe_{4.9}Ni_{0.08}O_{12}$ and $Y_3Fe_{4.9}Mo_{0.1}O_{12}$, which showed that the x = 0.04 sample achieved an optimal balance between thermal sensitivity and electrical insulation, promising for bolometer applications in a wide spectral range.

Keywords: Yttrium Iron Garnet (YIG), Mo^{5+} doping, Bolometric response, Near-infrared detection, Photothermal sensitivity.

* Corresponding author.
E-mail address: nguyet.daothithuy@hust.edu.vn

https//doi.org/10.25073/2588-1124/vnumap.5068

1. Introduction

Bolometers are among the most important thermal radiation detection devices today, especially useful in applications such as uncooled infrared detection, thermal imaging, laser measurement, security devices, and astronomical research [1-4]. Bolometers operate based on the phenomenon of increased heat in an absorbing material when exposed to electromagnetic radiation, which changes its electrical resistance and generates an electrical signal [1, 2, 5]. In the trend of modernizing non-contact sensor systems, uncooled bolometers are becoming an attractive option due to their low cost, wide spectral resolution, and high integration capability [1, 2, 4].

In the near-infrared (NIR: 750–1400 nm) region, the requirements for bolometric materials become even more stringent due to low photon energy and high background noise [6, 7]. Although traditional materials like VO_x, a-Si:H, or TiO_2 have certain sensitivities, they often face limitations in thermal stability, response time, and the ability to detect weak signals [6, 8, 9]. Therefore, developing new oxide materials with tunable conductivity, high thermal sensitivity, and long-term stability in the NIR region is a pressing research direction [6-8, 10-12].

The operating mechanism of bolometers is primarily based on three physical factors: i) The temperature coefficient of resistance (TCR), which reflects thermal sensitivity; ii) The photocurrent (I_{ph}), which represents the ability to generate a signal upon photon absorption; and iii) The noise equivalent power (NEP), which reflects the smallest detectable signal threshold [2, 3, 13]. These factors depend on the material's electronic characteristics, such as activation energy, resistance, doping level, and microstructural properties, including grain size, defect density, and inter-grain connectivity [2, 13, 14]. Therefore, the controlled tuning of electronic and microstructural properties is key to enhancing bolometric performance [2, 13-15].

Yttrium iron garnet (YIG, formula Y3Fe5O12) is a magnetic dielectric oxide material with a stable lattice structure, good thermal conductivity, low conductivity at room temperature, and tunable electrical properties through doping [16-18]. Although YIG is typically known in the fields of magnetic and photonic materials, it has recently attracted attention as a potential platform for bolometer sensors operating in the NIR region [16, 19,2 0]. Among various dopants, the Mo^{5+} ion (with a higher valence than Fe^{3+}) is expected to bring significant improvements. First, Mo^{5+} can tune the bandgap by creating intermediate energy levels, which aids in NIR photon absorption. Second, the presence of Mo^{5+} can promote the formation of Fe^{2+} to maintain charge neutrality, thereby increasing the carrier density. Third, Mo^{5+} contributes to improving the lattice structure, reducing defects, and minimizing background noise. Previous studies have shown that the concentration of Mo^{5+} doping strongly affects the electro-optical properties of YIG, but the optimal doping level remains an open question that needs clarification [16, 17].

In this context, this study focuses on investigating the bolometric characteristics of a $Y_3Fe_{5-x}Mo_xO_{12}$ ($x = 0.04$) sample, synthesized by the sol-gel method, and comparing it with a sample with a higher Mo concentration ($x = 0.1$) and a Ni^{2+}-doped YIG sample ($x = 0.08$). The goal is to determine the mechanism by which the Mo^{5+} concentration affects the sensor's performance, thereby evaluating its practical applicability in uncooled infrared thermal sensors.

2. Experiment

2.1. Material Synthesis

The molybdenum-doped YIG sample ($Y_3Fe_{4.96}Mo_{0.04}O_{12}$) was synthesized using a modified sol-gel method. First, Y_2O_3 (99.9%) and $Fe(NO_3)_3{\cdot}9H_2O$ (99.9%) were separately dissolved in hot 1 M HNO_3

solution to form 1 M Y^{3+} and Fe^{3+} ion solutions. Mo^{5+} was introduced into the system using a 0.1 M $MoCl_5$ solution in 1 M HNO_3 (yellow in color). The metal solutions were mixed in the molar ratio of [Y]:[Fe]:[Mo]=3:4.96:0.04. Next, 3 M citric acid was added in a molar ratio of three times the total amount of cations. The mixture was continuously stirred at 80 °C until a homogeneous gel was formed. The gel was then dried at 130 °C for 12 hours to produce a porous xerogel, which was then pre-ground with an agate mortar. The calcination process was carried out at 900 °C and 1000 °C for 5 hours to obtain crystalline $Y_3Fe_{4.96}Mo_{0.04}O_{12}$ powder.

2.2. Structural and Microstructural Analysis

The crystalline structure of the samples was determined by X-ray diffraction (XRD) using a Siemens D5005 (Bruker, Germany) diffractometer with Cu-Kα radiation (λ = 1.5406 Å). The XRD data were processed using SmartLab Studio II software to identify phases and determine lattice parameter values. Morphology and grain size were investigated by scanning electron microscopy (SEM, Jeol JCM 7000). Elemental composition was determined by inductively coupled plasma-atomic emission spectrometry (ICP–AES, Thermo Fisher ICP–IRIS). Raman spectra were measured using a Renishaw Invia microscope with a 514 nm laser at 2 mW power in the range of 110–800 cm^{-1}.

2.3. Electrical and Bolometric Properties Measurement

The powder sample was mixed with a PMMA polymer solution and deionized water to form a homogeneous suspension (0.3 g YIG powder, 3 g PMMA, 200 ml water). This suspension was drop-casted onto an interdigitated platinum electrode array on an alumina substrate (electrode gap and width of 200 μm). After each deposition (5 μl), the sample was dried at 70 °C for 10 minutes and thermally treated at 350 °C for 20 minutes. This process was repeated five times to create a uniform sensing layer. The device was fixed on a copper block and maintained at 300 K throughout the measurement.

Current-voltage (*I–V*) characteristics were recorded in the 300–425 K range using a Keithley 2602B measurement unit. Parameters such as room temperature resistance (R_0), temperature coefficient of resistance (TCR), and activation energy (ΔE) were extracted from the obtained characteristic curves.

Photo-current response was investigated using a modulated monochromatic light source system (Zahner) in the wavelength range of 315–1010 nm, with a square wave signal at 0.1 Hz frequency and a power density of 25 μW/mm². The total optical power illuminating the sensing area was approximately 125 μW. The noise current was measured to determine the noise equivalent power (NEP) and specific detectivity (D^*).

All sample fabrication and standard measurement procedures (including structural, morphological, and basic electrical characterization) were conducted at the Electronic Materials Laboratory, School of Materials Science, Hanoi University of Science and Technology (HUST). The ICP-AES measurements were carried out at the Vietnam Institute of Geosciences and Mineral Resources.

3. Results

Figure 1 shows the X-ray diffraction (XRD) patterns of the $Y_3Fe_{5-x}Mo_xO_{12}$ samples with Mo concentrations x = 0 and 0.04. All samples exhibit characteristic peaks of a cubic garnet phase, with no secondary phases appearing, which proves that the synthesis process produced a single-phase material [21, 22]. When doped with Mo^{5+} (x = 0.04), the diffraction peaks shift slightly towards a smaller 2θ angle, reflecting the phenomenon of lattice expansion. Rietveld refinement results show that the lattice constant slightly increases from 12.3756 Å (x = 0) to 12.3781 Å (x = 0.04) [21, 22].

This increase initially seems contradictory to predictions based on ionic size, as Mo^{5+} ($r \approx 0.61$ Å) is smaller than Fe^{3+} ($r \approx 0.645$ Å) and would be expected to cause lattice contraction when substituted into the Fe site [23]. However, to balance the charge due to the higher valence of Mo^{5+}, some of the Fe^{3+} ions in the lattice may be reduced to Fe^{2+} ($r \approx 0.78$ Å) [17, 23]. The appearance of Fe^{2+}, with its significantly larger radius, can lead to lattice expansion, which counteracts or even outweighs the lattice contraction effect of Mo^{5+}. Therefore, the observed slight increase in lattice constant is most likely the result of a coordinated effect of two opposing factors, with the influence of Fe^{2+} being dominant [17, 23].

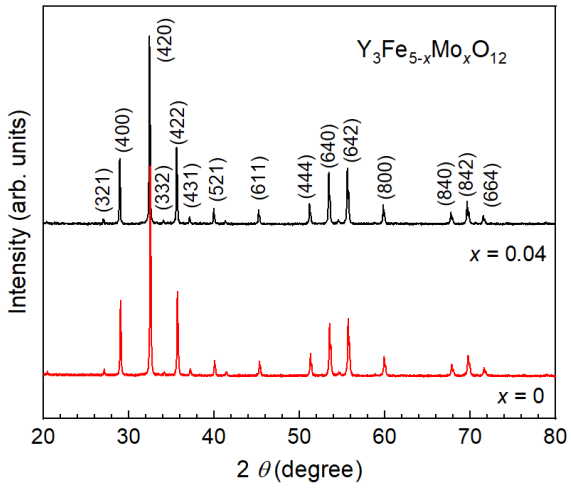

Figure 1. XRD patterns of $Y_3Fe_{5-x}Mo_xO_{12}$ samples ($x = 0$ and 0.04).

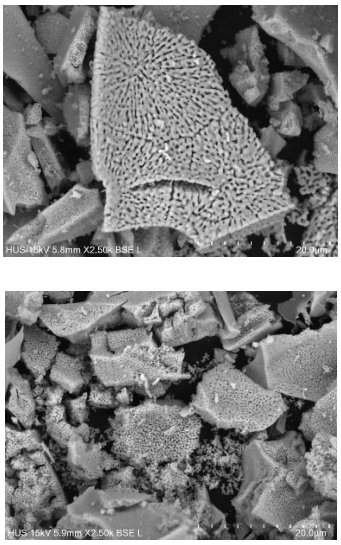

Figure 2. SEM images of the samples $x = 0$ (upper) and $x = 0.04$ (lower). The distance between the two white scale bars at the corner of the image represents 2 μm.

Figure 2 presents SEM images of the surface of samples with Mo doping levels of $x = 0$ and $x = 0.04$. The SEM images show a clear change in morphology upon Mo^{5+} doping. The undoped sample ($x = 0$) consists of large, plate-like particles with an estimated size from 5 to over 12 μm, exhibiting an elongated shape and a porous structure oriented in clear radial patterns, which reflects an orderly and uniform crystallization process. In contrast, the Mo^5-doped sample ($x = 0.04$) consists of plates that are distinctly fragmented into smaller pieces (approximately 2–8 μm). The surface shows a dense distribution of random pores and numerous fine particles of a few hundred nanometers attached to the surface. The pore size ranges from a few hundred nanometers to less than 1 μm, suggesting that the oriented crystallization process was interrupted, and also indicating an increase in lattice defects due to the doping effect of Mo^{5+}. The fragmented structure with a larger surface area is expected to improve optical absorption and heat transfer, which is favorable for bolometric applications.

Figure 3 shows the FTIR spectra of $Y_3Fe_{5-x}Mo_xO_{12}$ samples ($x = 0$ and 0.04). The main absorption bands appear in the range of 550–600 cm^{-1} (octahedral Fe–O bending vibrations) and 600–700 cm^{-1} (tetrahedral Fe–O stretching vibrations), which are characteristic of the garnet lattice [24–26]. Upon Mo^{5+} doping, these bands shift slightly towards higher wavenumbers and their amplitudes decrease, indicating a partial substitution of Fe^{3+} at the octahedral sites and a local distortion of the crystal lattice [24,25]. This shift is attributed to the substitution of Fe^{3+} ($r \approx 0.645$ Å) by the smaller Mo^{5+} ion ($r \approx 0.61$ Å) at the octahedral sites, causing local lattice compression and a shortening of the Fe–O bonds, which

increases the bonding force constant [24, 25]. Additionally, the distortion of the FeO_6 octahedra and FeO_4 tetrahedra also contributes to an increase in the bonding force, leading to higher vibrational frequencies (shifted to higher wavenumbers) [24-26]. Combined with the morphological observations from the SEM images, it is evident that Mo^{5+} not only affects the crystallization kinetics but also contributes to the local structural stability of the crystal lattice [24].

Figure 4 illustrates the *I–V* characteristics of the $Y_3Fe_{5-x}Mo_xO_{12}$ ($x = 0.04$) sample in dark conditions at different temperatures. It can be observed that the current increases faster at higher temperatures, reflecting the thermally activated semiconducting nature of the material. The *I–V* characteristics of the $Y_3Fe_{5-x}Mo_xO_{12}$ ($x = 0.04$) sample at various temperatures show two distinct conduction regions. In the low voltage region (<1 V), the current increases linearly with voltage, which reflects the Ohmic conduction mechanism dominated by free carriers [27, 28]. In the range of 1–3.5 V, the *I–V* curve becomes noticeably non-linear, suggesting the onset of a space-charge-limited conduction (SCLC) mechanism where charge traps dominate the transport process [27-29]. The SCLC mechanism occurs when the current is limited by the accumulation of space charge rather than the number of injected carriers; this theory is detailed in classic literature such as Rose (1955) [28], and Sze & Ng (2006) [29]. At low voltages, conduction follows the Ohmic mechanism; as the voltage increases, charge traps (from lattice defects, impurities, grain boundaries, multi-valent cations like Mo^{5+}, Fe^{2+}, or secondary phases) capture carriers, leading to a non-linear *I–V* relationship ($I \propto V^n$, $n > 2$) [28, 29]. When the traps are filled (trap-filled limit), the current increases almost linearly due to the predominance of free carriers; this concept is well-described in typical examples on metal oxides by Bubel et al., [27]. Notably, from approximately 3.5–5 V, the *I–V* relationship returns to a nearly linear state, indicating that the charge traps have been filled, leading to the predominance of free carriers and a steady increase in current with voltage [27]. At 5 V, the current reaches approximately 6.8×10^{-5} A at 300 K, reflecting a high carrier density and good electrical stability of the material, which is suitable for bolometric sensor applications requiring high thermal sensitivity [27].

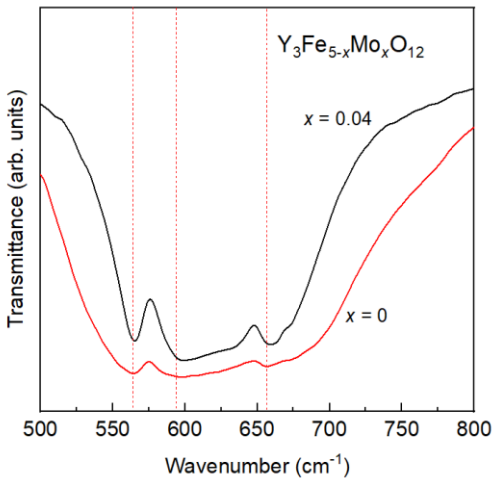

Figure 3. FTIR spectra of the $Y_3Fe_{5-x}Mo_xO_{12}$ samples. The dotted lines mark the centers of the absorption bands for the sample x = 0.

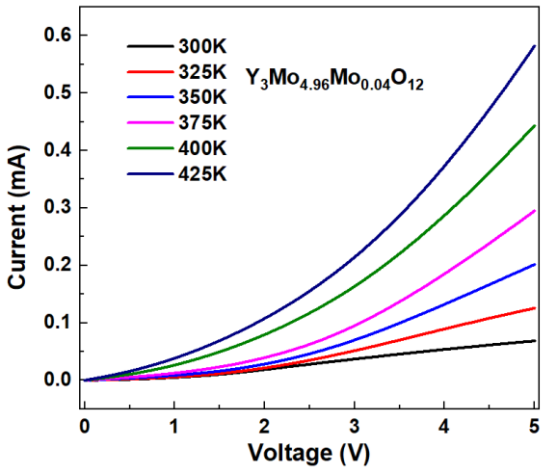

Figure 4. Current-voltage (*I–V*) characteristics of $Y_3Fe_{5-x}Mo_xO_{12}$ ($x = 0.04$) sample in darkness at different temperatures.

The resistance of the sample at various temperatures was determined from the linear segment of the current-voltage (*I–V*) characteristic in the high voltage region, where the *I–V* relationship obeys Ohm's

law. Specifically, at each temperature, the resistance value was calculated by taking the slope of the linear segment using the expression $R = \Delta V/\Delta I$.

Figure 5 shows the temperature dependence of resistance (R–T) for the x = 0.04 sample. The $Y_3Fe_{4.96}Mo_{0.04}O_{12}$ sample exhibits a marked decrease in resistance as the temperature increases from 300 K to 425 K, reflecting the typical behavior of a semiconductor material. The variation of resistance with temperature is consistent with a thermally activated conduction mechanism, which can be described by the Arrhenius function [30]:

$$R(T) = R(T_0)e^{-\frac{\Delta E}{k_B}\left(\frac{1}{T}-\frac{1}{T_0}\right)} \quad (1)$$

where $R(T)$ is the resistance at temperature T, $R(T_0)$ is the resistance at the reference temperature T_0 (usually room temperature), ΔE is the activation energy, and k_B is the Boltzmann constant. The inset in Figure 5 displays the corresponding temperature coefficient of resistance (TCR), calculated from the derivative of the resistance with respect to temperature using the formula:

$$\mathrm{TCR} = -(1/R) \cdot (dR/dT) \quad (2)$$

where R is the resistance at temperature T and dR/dT is the rate of change of resistance with temperature.

The calculation results show that the TCR of this sample has a value of 3.9 %/K at 300 K. The corresponding electrical parameters are presented in Table 1.

Figure 6 shows the photoresponse of the $Y_3Fe_{5-x}Mo_xO_{12}$ sample with x = 0.04 under different illumination wavelengths in the range from 281 nm to 1010 nm, measured at a bias voltage of 5 V. The results indicate that the photocurrent gradually increases with the illumination wavelength, from a very small value in the UV region to a maximum value in the NIR region, particularly at 914 nm. This increase reflects the material's more efficient absorption and conversion of photon energy in the visible and NIR light regions, suggesting its high potential for application in photothermal sensor devices operating in this spectral range.

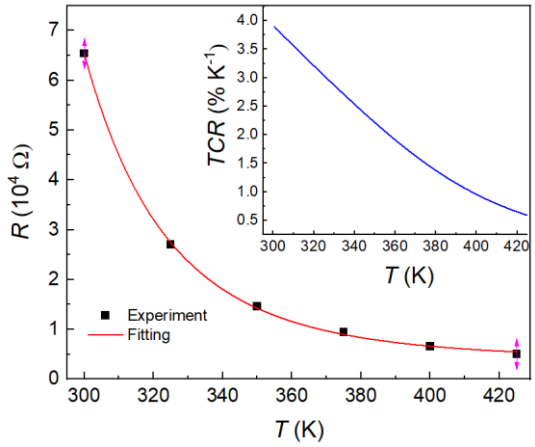

Figure 5. Resistance (R) of $Y_3Fe_{5-x}Mo_xO_{12}$ sample (x = 0.04) as a function of temperature. The inset shows the temperature coefficient of resistance (TCR) of the sample as a function of temperature.

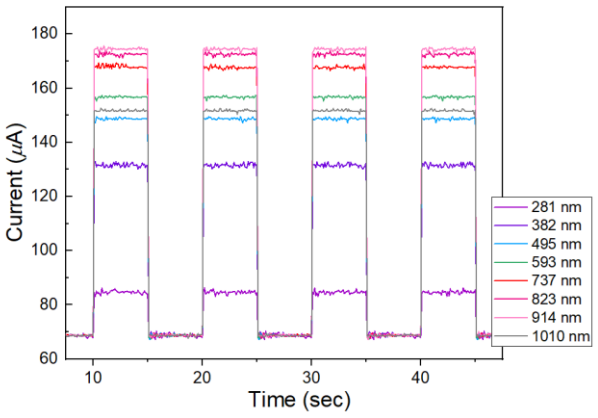

Figure 6: Photocurrent response (I_{ph}) of $Y_3Fe_{5-x}Mo_xO_{12}$ sample (x = 0.04) at a bias voltage of 5 V under different illumination wavelengths (315–1010 nm).

Figure 7 illustrates the dependence of the photocurrent (I_{ph}) on the excitation photon energy at a 5 V bias voltage. The photoresponse of the $Y_3Fe_{4.96}Mo_{0.04}O_{12}$ sample was investigated in a wide wavelength range from ultraviolet (UV), through visible (VIS), to near-infrared (NIR). The photocurrent

is defined as the difference between the current under illumination (I_{ON}) and the current in the dark (I_{OFF}), reflecting the material's ability to convert photons into electrical signals. The results show that, in the UV region (281 nm wavelength), I_{ph} only reaches a very low value (~0.016 mA), demonstrating the material's weak response to high-energy photons. However, as the wavelength gradually increases towards the visible and near-infrared regions, the photocurrent increases significantly and reaches a maximum value (~3.83 mA) at a wavelength of 914 nm, indicating the highest photon absorption and conversion efficiency in this region. The increasing trend of Iph from UV to NIR suggests a prominent role for energy levels related to the Fe^{3+} ion in the garnet crystal lattice, particularly the $^6A_1g \rightarrow {}^4T_1g$ electron transition at the octahedral site [31], along with the photoluminescence quenching effect at long wavelengths [32], which contributes to the increased efficiency of photothermal conversion.

The responsivity (R_i) quantifies the photo-sensitivity of the $Y_3Fe_{5-x}Mo_xO_{12}$ (x = 0.04) sample, reflecting its efficiency in converting light into an electrical signal. It is calculated using the formula: $R_i = I_{ph}/P$, where P is the incident radiation power (W). The calculated sensitivity results at various photon excitation energies are also presented in Figure 7. According to the data, R_i peaks at 848 mA/W at a wavelength of 914 nm, indicating the sample's efficient absorption and conversion of photons in the near-infrared (NIR) region. At other wavelengths, such as 737 nm (792 mA/W), 823 nm (832 mA/W), and 953 nm (704 mA/W), R_i also remains high, confirming that the NIR region is the optimal operating range. In the visible (VIS) region, R_i values are still quite good, reaching 640 mA/W (495 nm) and 504 mA/W (382 nm). Conversely, in the ultraviolet region (281 nm), R_i only reaches 128 mA/W. This distribution reflects an energy band structure that is favorable for absorbing medium-to-low energy photons, which is associated with the Fe^{2+}/Mo^{5+} centers. With performance comparable to or exceeding many traditional bolometer materials like VO_x [33] or a-Si: H [31], the Mo-doped YIG sample shows great potential for high-sensitivity optical sensors and thermal detectors.

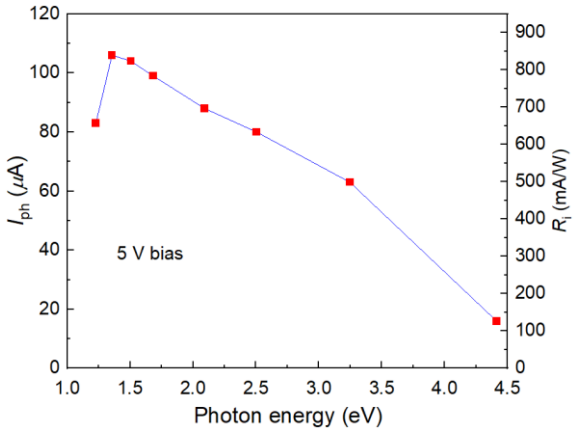

Figure 7. Photocurrent (I_{ph}) and responsivity (R_i) of the $Y_3Fe_{5-x}Mo_xO_{12}$ sample (x = 0.04) as a function of excitation photon energy under bias voltage 5 V.

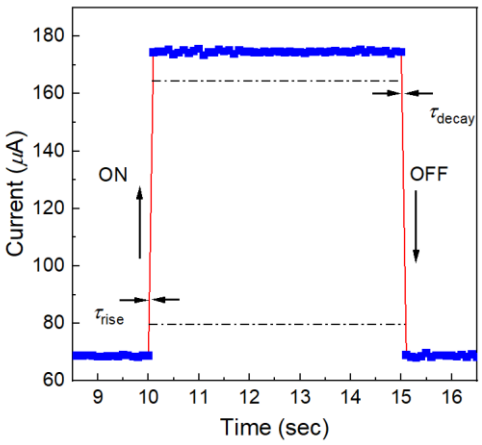

Figure 8. Normalized photocurrent response of $Y_3Fe_{5-x}Mo_xO_{12}$ sample (x = 0.04) under pulsed light illumination at a bias voltage of 3 V. Rise time (τ_{rise}) and fall time (τ_{fall}) are 76 and 72 ms, respectively.

Figure 8 displays the normalized transient photoresponse of the $Y_3Fe_{5-x}Mo_xO_{12}$ sample with x = 0.04 when illuminated with pulsed light at a bias voltage of 5 V. The obtained curve shows that the photocurrent signal exhibits good reproducibility across the light on/off cycles, with a stable and nearly zero-delay amplitude. This reflects the material's fast response and high sensitivity to changes in the input light, proving that the sample operates stably under varying illumination conditions, making it

highly suitable for real-time bolometric sensing applications. The rise time (τ_{rise}) and fall time (τ_{fall}) are approximately 76 and 72 ms, respectively, indicating a fast response—a critical factor for high-speed bolometer sensors.

Noise Equivalent Power (NEP) is a quantity that characterizes an optical sensor's ability to detect weak signals. It is determined by the formula NEP = I_n/R_i, where I_n is the noise current density. A smaller NEP value indicates a more sensitive sensor, meaning it can detect weaker radiation signals. For the sample under investigation, the NEP is in the range of $(2.86–5.73)\times10^{-8}$ W·Hz$^{-1/2}$.

The detectivity (D^*) is calculated by the formula $D^* = R_i$/NEP. A higher D^* reflects a better ability to detect signals in noisy conditions.

Figure 9 illustrates the dependence of D^* and NEP (inset) on the photon excitation energy for the $Y_3Fe_{5-x}Mo_xO_{12}$ sample ($x = 0.04$). The data shows that the detectivity of this material changes with the excitation wavelength, clearly reflecting the effectiveness of signal detection under the influence of noise. Within the surveyed energy range, D^* fluctuates from 7.8×10^7 to 5.4×10^8 cm·Hz$^{1/2}$·W^{-1}, with the maximum value at 914 nm, which coincides with the peak of the photocurrent (I_{ph}).

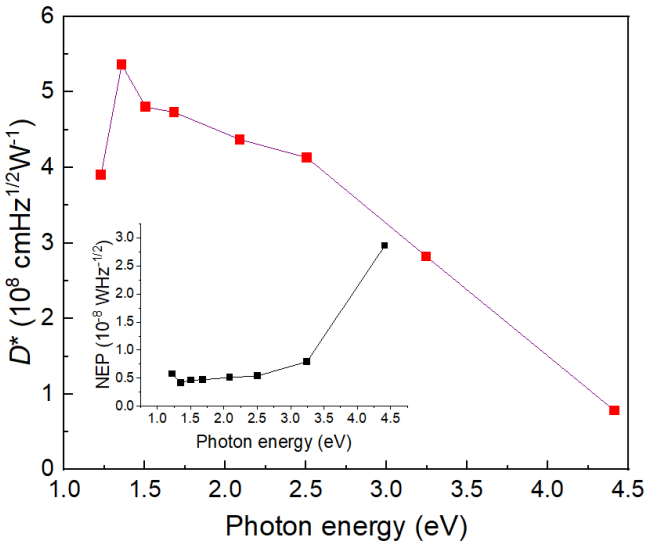

Figure 9. Normalized detectivity (D^*) of $Y_3Fe_{5-x}Mo_xO_{12}$ sample ($x = 0.04$) as a function of excitation photon energy. The inset displays the Noise Equivalent Power (NEP) of the sample.

The combination of NEP and D^* shows that although the smallest NEP occurs in the UV region (281 nm), the D^* at this wavelength is low due to the very small value of R_i. Conversely, at 914 nm, both I_{ph} and R_i are high, while the NEP remains low, leading to a maximum D^* value. This confirms that the 914 nm wavelength is optimal for signal detection efficiency and highlights the potential applications of Mo-doped YIG material in thermophotovoltaic sensors operating in the near-infrared (NIR) region.

4. Discussion

To evaluate the bolometric efficiency of YIG materials doped with different elements, we performed a comparative analysis of a series of representative samples representing various modifications of the garnet lattice structure, drawing upon experimental results from recent studies. For this purpose, we

chose three YIG material samples for comparison: $Y_3Fe_{5-x}Mo_xO_{12}$ (with $x = 0.04$ and $x = 0.1$ [34]), and the $Y_3Fe_{4.92}Ni_{0.08}O_{12}$ (Ni-doped YIG) sample [35]. Crucially, these comparison samples were fabricated and characterized by our research group under the identical synthesis conditions as the sample reported in this current study. The electrical and optical parameters relevant to the bolometric effect for these samples are summarized in Table 1.

In terms of electrical properties, the $Y_3Fe_{4.9}Mo_{0.1}O_{12}$ ($x = 0.1$) sample exhibited the lowest room temperature resistance (R_0) (~7.3×10^4 Ω) and the highest photocurrent (I_{ph}) (~270 μA), indicating superior electrical conductivity and a strong photothermal effect. Conversely, the Ni-doped YIG sample had the highest resistance (2.5×10^6 Ω) and the lowest photocurrent (~83 μA), reflecting a poorer bolometric performance. The Mo-doped sample with $x = 0.04$ achieved intermediate values, with R_0 around 6.54×10^4 Ω and Iph approximately 106 μA.

Regarding the activation energy (ΔE), the $x = 0.04$ sample has the highest value (0.32 eV), indicating a well-ordered crystal structure with few electronic defects, which helps to maintain its insulating state at low temperatures. Meanwhile, both of the other samples ($x = 0.1$ and Ni-doped) have a low ΔE (0.19 eV), reflecting the presence of intermediate impurity levels generated during the doping process, which contributes to lowering the potential barrier and increasing conductivity.

Table 1. Comparison of characteristic electrical and optical parameters for the bolometric effect of YIG samples doped with Ni and Cu, with the values measured at room temperature; the values of I_{ph}, R_i, and D^* are determined at an excitation wavelength of 914 nm, corresponding to the peak position of the optical response, and an incident power of 125 μW.

Parameters	Ni-doped YIG ($x = 0.08$) [34]	Mo-doped YIG ($x = 0.04$)	Mo-doped YIG ($x = 0.1$) [35]
Resistence (R_0) [Ω]	2.5×10^6	6.54×10^4	7.3×10^4
Activation energy (ΔE) [eV]	0.19	0.32	0.19
TCR [%·K^{-1}]	2.4	3.9	2.5
Photocurrent (I_{ph}) [μA]	~83	~106	~270
Noise spectral density (I_n) [A·Hz$^{-1/2}$]	1.25×10^{-6}	3.54×10^{-6}	3.81×10^{-6}
NEP [W·Hz$^{-1/2}$]	0.5×10^{-5}	4.17×10^{-9}	0.25×10^{-8}
Responsivity (R_i) [mA/W]	370	848	~2160
Detectivity (D^*) [cm·Hz$^{1/2}$/W]	~3.5×10^7	~2.5×10^8	~5.2×10^8

The resistance at room temperature (R_0) not only reflects the intrinsic electronic properties of the material but is also strongly influenced by its microstructure, such as grain size, grain boundary density, and the degree of sintering. The Ni-doped sample has the highest R_0, suggesting that the crystal lattice was not effectively doped, and a large grain structure with poor inter-grain connectivity may exist. In contrast, the $x = 0.04$ sample has a lower resistance, which suggests that the doping level and microstructure have begun to support conduction. Notably, the $x = 0.1$ sample has the lowest R_0, indicating an effective combination of a high Mo doping level and a well-sintered grain structure, which reduces the electrical barrier at grain boundaries. Thus, the decreasing trend in R_0 is not only due to improved electronic states but also to the optimization of the material structure during the fabrication process.

The combined effect of ΔE and R_0 directly influences the photocurrent obtained (I_{ph}). Specifically, the $x = 0.1$ sample has a low ΔE and a small R_0, resulting in the highest I_{ph}. In contrast, the $x = 0.04$ sample has a reasonable R_0 but a high ΔE, so its I_{ph} is only at a medium level. The Ni-doped sample has a low ΔE but a very high R_0, which impedes charge carrier flow, leading to the lowest I_{ph}. This shows that to achieve a strong photocurrent, the material needs both a low conduction potential barrier and an optimal level of resistance.

The Noise Equivalent Power (NEP) is a quantity that evaluates the threshold of the weakest radiation signal that a sensor can detect, and it depends on both the electrical conductivity and the intrinsic noise level. The Ni-doped sample has the highest NEP (0.5×10^{-5} W·Hz$^{-1/2}$), mainly because high resistance increases Johnson noise. The $x = 0.04$ sample has a lower NEP (4.17×10^{-9} W·Hz$^{-1/2}$), reflecting a good balance between insulation and conductivity. The $x = 0.1$ sample achieves the lowest NEP (0.25×10^{-8} W·Hz$^{-1/2}$), which demonstrates the optimization in noise control and improved conductivity.

The photoresponsivity (R_i) is a function of I_{ph}, NEP, R_0, and ΔE. With a large photocurrent, a low potential barrier, and low noise, the $x = 0.1$ sample achieves the highest R_i (~2160 mA/W). The $x = 0.04$ sample has a medium R_i (848 mA/W), while the Ni-doped sample only reaches ~370 mA/W due to a combination of a weak I_{ph} and high noise. Thus, to achieve a high R_i, the material needs to simultaneously ensure good conductivity, charge carrier activation capability, and effective noise control.

Finally, the overall parameter of detectivity (D^*), which characterizes the ability to detect a weak signal in noisy conditions, reflects the overall effectiveness of the material. The $x = 0.1$ sample continues to show superiority with the highest D^* (~5.2×10^8 cm·Hz$^{1/2}$·W^{-1}), due to the simultaneous convergence of optimal physical factors: low resistance, low potential barrier, strong I_{ph}, low NEP, and high R_i. The $x = 0.04$ sample gives a medium D^* value (~2.5×10^8 10^8 cm·Hz$^{1/2}$·W^{-1}) by maintaining a balance between these factors, while the Ni-doped sample has the lowest D^* (~3.5×10^7 10^8 cm·Hz$^{1/2}$·W^{-1}) due to limitations in photocurrent, conductivity, and noise levels.

In summary, among the three samples studied, the $Y_3Fe_{4.9}Mo_{0.1}O_{12}$ material shows superior bolometric performance due to the simultaneous integration of optimal physical factors: good conductivity, high thermal sensitivity, effective noise control, and a strong photo-signal. This makes it a highly promising candidate for near-infrared thermophotovoltaic sensors.

5. Conclusion

The $Y_3Fe_{4.96}Mo_{0.04}O_{12}$ sample exhibits impressive bolometric performance due to a harmonious combination of high activation energy, suitable resistance, and a large TCR, which enhances thermal sensitivity. Although the photocurrent and responsivity have not reached the maximum levels of the $x = 0.1$ sample, the low NEP and stable characteristics of the $x = 0.04$ sample still ensure high detectivity, especially in the near-infrared region. Compared to the Ni-doped sample ($x = 0.08$), the $x = 0.04$ sample is clearly superior in terms of photocurrent, sensitivity, and noise stability. These results confirm that low-level Mo^{5+} doping ($x = 0.04$) is an effective strategy for enhancing the bolometric properties of YIG, while maintaining a stable lattice structure and being suitable for sensors operating under real-world conditions.

Acknowledgments

This research was funded by the Ministry of Education and Training of Vietnam, coded B2024-BKA-23.

References

[1] P. Richards, Bolometers for Infrared and Millimeter Waves, Journal of Applied Physics, Vol. 76, 1994, pp. 1-24, https://doi.org/10.1063/1.357128.

[2] Q. Zhang, R. Yan, X. Peng, Y.Wang, S. Feng, TiO_{2-x} Films for Bolometer Applications: Recent Progress and Perspectives, Materials Research Express, Vol. 9, No. 1, 2022, 012002, https://doi.org/10.1088/2053-1591/ac4327.

[3] R. Kokkoniemi, J. Girard, D. Hazra, A. Laitinen, J. Govenius, R. Lake, I. Sallinen, V. Vesterinen, M. Partanen, J. Tan, K. Chan, P. Hakonen, M. Möttönen, Bolometer Operating at the Threshold for Circuit Quantum Electrodynamics, Nature, Vol. 586, 2020, pp. 47-51, https://doi.org/10.1038/s41586-020-2753-3.

[4] B. Fisette, F. Généreux, D. Béland, P. Topart, M. Tremblay, Y. Desroches, M. Terroux, L. Marchese, C. Proulx, F. Picard, D. Dufour, A. Bergeron, F. Châteauneuf, C. Alain, Customized Packaged Bolometers in Niche Applications at INO, Proceedings of SPIE, 2018, pp. 10656, https://doi.org/10.1117/12.2303513.

[5] C. Jones, The General Theory of Bolometer Performance, Journal of the Optical Society of America, Vol. 43, 1953, pp. 1-14, https://doi.org/10.1364/JOSA.43.000001.

[6] S. Nandi, A. Misra, Carbon Nanotube-Based Uncooled Bolometers: Advances and Progress, ACS Materials Letters, Vol. 5, No. 1, 2023, pp. 249-274, https://doi.org/10.1021/acsmaterialslett.2c00680.

[7] M. Bartmann, M. Sistani, N. Luhmann, S. Schmid, E. Bertagnolli, A. Lugstein, J. Smoliner, Germanium Nanowire Microbolometer, Nanotechnology, Vol. 33, No. 24, 2022, pp. 245201, https://doi.org/10.1088/1361-6528/ac5aec.

[8] J. Shim, J. Lim, D. Geum, J. You, H. Yoon, J. Kim, W. Baek, J. Han, S. Kim, TiO_x/Ti/TiO_x Tri-Layer Film-Based Waveguide Bolometric Detector for On-Chip Si Photonic Sensor, IEEE Transactions on Electron Devices, Vol. 69, 2022, pp. 2151-2158, https://doi.org/10.1109/ted.2021.3132264.

[9] M. Khan, P. S. Moshkenani, M. Islam, O. Boyraz, J. Sullivan, Z. Yu, J. Lee, Selective and Efficient Infrared Detection by Plasmonically Heated Vanadium-Dioxide Nanowire, Proceedings of SPIE, Vol. 11462, 2020, pp. 114622S, https://doi.org/10.1117/12.2568971.

[10] Y. Huang, L. Wei, T. Chen, T. Xu, Y. Cai, Y. Guo, Y. Xie, Ultra-Low-Density Carbon Nanotube Aerogel Film for Fast and Sensitive Bolometric Sensing, ACS Applied Materials & Interfaces, Vol. 15, No. 9, 2023, pp. 12137-12145, https://doi.org/10.1021/acsami.2c20099.

[11] V. P. Krishnakumar, A. D. Mahapatra, V. Panwar, A. Mondal, C. Kumar, P. Kuma, A. Misra, Semiconductor Nanoparticle Anchored Single-Walled Carbon Nanotubes for a Bolometer, Langmuir, Vol. 40, No. 21, 2024, pp. 11023-11029, https://doi.org/10.1021/acs.langmuir.4c00393.

[12] Y. Wei, C. Chen, C. Tan, L. He, Z. Ren, C. Zhang, S. Peng, J. Han, H. Zhou, J. Wang, High-Performance Visible to Near-Infrared Broadband Bi_2O_2Se Nanoribbon Photodetectors, Advanced Optical Materials, Vol. 10, No. 23, 2022, pp. 2201396, https://doi.org/10.1002/adom.202201396.

[13] P. V. Yadav, I. Yadav, B. Ajitha, A. Rajasekar, S. Gupta, Y. A. K. Reddy, Dispatched Advancements of Uncooled Infrared Microbolometer Materials: A Review, Sensors and Actuators A: Physical, Vol. 342, 2022, pp. 113611, https://doi.org/10.1016/j.sna.2022.113611.

[14] A. Ainabayev, D. Mullarkey, B. Walls, D. Caffrey, K. Zhussupbekov, A. Zhussupbekova, C. Ilhan, A. Kaisha, P. Biswas, A. Tikhonov, O. Murtagh, I. Shvets, Epitaxial Grown VO_2 with Suppressed Hysteresis and Low Room Temperature Resistivity for High-Performance Thermal Sensor Applications. ACS Applied Nano Materials, Vol. 6, No. 4, 2023, pp. 2917-2927, https://doi.org/10.1021/acsanm.2c05297.

[15] R. Zhou, J. T. W. Yeow, Innovations in Bolometer Technology for Enhanced Terahertz Detection, IEEE Nanotechnology Magazine, Vo. 18, No. 5, 2024, pp. 4-13, https://doi.org/10.1109/MNANO.2024.3436328.

[16] A. D'Amico, A. Grilli, A. Paoletti, P. Paroli, A. Tucciarone, Doped Yttrium Iron Garnet for Thermistor-Bolometers, Materials Research Bulletin, Vol. 19, No. 3, 1984, pp. 347-354, https://doi.org/10.1016/0025-5408(84)90177-6.

[17] N. P. Duong, D. T. T. Nguyet, T. T. Loan, L. N. Anh, S. Soontaranon, W. Klysubun, T. T. V. Nga, Effects of Sn^{4+} Doping and Oxygen Vacancy on Magnetic and Electrical Properties of Yttrium Iron Garnet Prepared by Sol-Gel Method, Ceramics International, Vol. 47, No. 5, 2021, pp. 6442-6452, https://doi.org/10.1016/j.ceramint.2020.10.226.

[18] A. A. Bhosale, S. B. Somvanshi, V. D. Murumkar, K. M Jadhav, Influential Incorporation of RE Metal Ion (Dy^{3+}) in Yttrium Iron Garnet (YIG) Nanoparticles: Magnetic, Electrical, and Dielectric Behaviour, Ceramics International, Vol. 46, No. 10A, 2020, pp. 15372-15378, https://doi.org/10.1016/j.ceramint.2020.03.081

[19] A. D'Amico, P. Gasperis, A. Grilli, A. Paoletti, G. Petrocco, Calcium-Doped Yttrium Iron Garnet Films for Temperature Sensors, Thin Solid Films, Vol. 129, 1985, pp. 151-159, https://doi.org/10.1016/0040-6090(85)90103-8.

[20] A. D'Amico, P. de Gasperis, F. Giannini, V. Parisi, Novel Calcium-Doped Yttrium-Iron-Garnet Thermistor Bolometer In A Planar and Continuous Bridge Configuration, Electronics Letters, Vol. 20, No. 21, 1984, pp. 874-875, https://doi.org/10.1049/EL:19840593.

[21] S. Khanra, A. Bhaumik, Y. D. Kolekar, P. Kahol, K. Ghosh, Structural and Magnetic Studies of $Y_3Fe_{5-5x}Mo_{5x}O_{12}$, Journal of Magnetism and Magnetic Materials, Vol. 369, 2014, pp. 14-22, https://doi.org/10.1016/j.jmmm.2014.06.018.

[22] B. Isherwood, An X-ray Multiple Diffraction Study of Yttrium Iron Garnet Crystals, Journal of Applied Crystallography, Vol. 1, 1968, pp. 299-307, https://doi.org/10.1107/S0021889868005546.

[23] M. Hossain, M.N. Rhaman, M.M. Ali, N. Jahan, A. Momin, M. Rahman, M. Hakim, Novel Gadolinium (Gd) and Chromium (Cr) Co-Doped Yttrium Iron Garnet ($Y_3Fe_5O_{12}$) Nanoparticles, Arabian Journal for Science and Engineering, Vol. 49, 2024, pp. 9967-9982, https://doi.org/10.1007/s13369-023-08613-y.

[24] M. H. El Makdah, M. H. El-Dakdouki, R. Mhanna, F. Al Boukhari, R. Awad, Effects of Neodymium Substitution on the Structural, Optical, and Magnetic Properties of Yttrium Iron Garnet Nanoparticles, Applied Physics A, Vol. 127, No. 304, 2021, https://doi.org/10.1007/s00339-021-04466-0.

[25] A. Bhalekar, L. Singh, Structural and Magnetic Studies of Aluminum-Substituted YIG Nanoparticles Prepared by a Sol-Gel Route, Brazilian Journal of Physics, Vol. 49, 2019, pp. 636-645, https://doi.org/10.1007/s13538-019-00690-5.

[26] A. Hofmeister, K. Campbell, Infrared Spectroscopy of Yttrium Aluminum, Yttrium Gallium, and Yttrium Iron Garnets, Journal of Applied Physics, Vol. 72, 1992, pp. 638-646, https://doi.org/10.1063/1.351846.

[27] S. Bubel, N. Mechau, H. Hahn, R. Schmechel, Trap States and Space Charge Limited Current in Dispersion Processed Zinc Oxide Thin Films, Journal of Applied Physics, Vol. 108, 2010, pp. 124502, https://doi.org/10.1063/1.3524184.

[28] C. Kee, Y. Ang, L. Ang, Trap-Limited Space-Charge Limited Current in 2D Thin Film Dielectric, IEEE International Conference on Plasma Science (ICOPS), 2022, pp. 1-2, https://doi.org/10.1109/ICOPS45751.2022.9813170.

[29] R. Boer, A. Morpurgo, Influence of Surface Traps on Space-Charge Limited Current, Physical Review B, Vol. 72, 2005, pp. 073207, https://doi.org/10.1103/PhysRevB.72.073207.

[30] R. E. Jr. Fontana, D. J. Epstein, AC Hopping Conductivity in Silicon-Doped Yttrium-Iron Garnet, Materials Research Bulletin, Vol. 6, 1971, pp. 959-966, https://doi.org/10.1016/0025-5408(71)90074-2.

[31] S. H. Wemple, S. L. Blank, J. A. Seman,mW. A. Biolsi, Optical Properties of Epitaxial Iron Garnet Thin Films, Physical Review B, Vol. 9, No. 5, 1974, pp. 2134-2144, https://doi.org/10.1103/PhysRevB.9.2134.

[32] A. Saroha, K. L. Ganapathi, M. Sadhasivam, K. G. Pradeep, M. S. R. Rao, White-Light Emission from Yttrium Iron Garnet (YIG), APL Materials, Vol. 11, No. 4, 2023, pp. 041116, https://doi.org/10.1063/5.0135423.

[33] S. Balendhran, M. Taha, S. Wang, W. Yan, N. Higashitarumizu, D. Wen, N. S. Azar, J. Bullock, Crozier, P. Mulvaney, A. Javey, K. B. Crozier, Flexible Vanadium Dioxide Photodetectors for Visible to Longwave Infrared Detection at Room Temperature, Advanced Functional Materials, Vol. 33, No. 43, 2023, pp. 2301790, https://doi.org/10.1002/adfm.202301790.

[34] N. P. Duong, D. T. T. Nguyet, N. M. Vuong, T. T. Loan, N. T. Nguyen, Sol–Gel Synthesis and Multifunctional Characterization of Mo-Substituted YIG for High-Sensitivity Photodetection, Journal of Alloys and Compounds, Vol. 1043, 2025, pp. 184235, https://doi.org/10.1016/j.jallcom.2025.184235.

[35] N. P. Duong, D. T. T. Nguyet, D. T. Hieu, L. N. Anh, Ni-Doped Yttrium Iron Garnet: A High-Performance Thermistor-Bolometer for UV to Near-Infrared Detection, Sensors and Actuators A: Physical, Vol. 391, 2025, pp. 116629, https://doi.org/10.1016/j.sna.2025.116629.